scientific reports

Check for updates

OPEN

Influence of boundary conditions and blood rheology on indices of wall shear stress from IVUS-based patient-specific stented coronary artery simulations

R. Patrick McCarthy[1✉], Peter J. Mason[2,5], David S. Marks[2] & John F. LaDisa Jr.[1,2,3,4]

The long-term clinical efficacy of coronary stents is limited by restenosis. Coronary stenting results in altered arterial geometry, local blood flow patterns, and wall shear stress (WSS), all of which can influence restenosis. Computational fluid dynamics (CFD) simulations employ assumptions about blood properties and boundary conditions, which also influence WSS alterations from stenting. Our objective was to evaluate three common assumptions applied with stented coronary artery CFD simulations (inlet velocity profile, outlet boundary conditions, and viscosity) to provide insight for future studies. A patient-specific right coronary artery was reconstructed from intravascular ultrasound and computed tomography imaging. Time-averaged WSS (TAWSS) and oscillatory shear index (OSI) were compared for CFD simulations using parabolic and Womersley ($\alpha = 2.5$) velocity profiles and Newtonian versus non-Newtonian (Carreau-Yasuda) viscosity. TAWSS and OSI differences were quantified for 5-element lumped parameter network (LPN) outlet boundary conditions as compared to a 3-element Windkessel approach previously applied by neglecting ventricular contraction. Differences in velocity profiles were negligible beyond two diameters from the inlet. Differences between Womersley inlet 3-element and 5-element LPNs were ~ 5% for TAWSS and ~ 200% for OSI, and most pronounced near stent struts. OSI differences were due to pressure differences between outlet boundary conditions inducing different near-wall velocity gradients. TAWSS differences between viscosity models were greatest near struts (~ 100%). Collectively these results suggest certain assumptions commonly applied for simulations of stented coronary arteries have a greater impact on TAWSS and OSI than others, with outlet boundary conditions being paramount, followed by viscosity model and inlet velocity profile.

The evolution and proven efficacy of bare-metal and drug-eluting stents in the treatment of obstructive coronary artery disease has led to percutaneous coronary intervention being the most common form of revascularization. However, the long-term durability of coronary stents is limited by restenosis and, to a lesser extent, late stent thrombosis[1] resulting in >200,000 repeat procedures in the US annually[2]. The factors contributing to restenosis are not fully understood, but WSS indices have been implicated since stenting alters artery geometry and local blood flow patterns[3]. Adverse WSS also correlates with neointimal hyperplasia (the main component of restenosis) and inhibits endothelialization that protects against late stent thrombosis[4–6].

Computational fluid dynamics (CFD) has become a valuable tool for assessment of WSS indices due to its noninvasive nature and potential for results with high spatiotemporal resolution. This is particularly important in the setting of stents with linkages (i.e., struts) on the order of 50 microns that impose local geometric perturbations. Importantly, CFD simulations employ assumptions regarding blood rheology and boundary conditions that influence WSS indices.

[1]Department of Biomedical Engineering, Medical College of Wisconsin and Marquette University, Milwaukee, WI 53226, USA. [2]Department of Medicine; Division of Cardiovascular Medicine, Medical College of Wisconsin, Milwaukee, WI 53226, USA. [3]Department of Pediatrics; Section of Cardiology, Herma Heart Institute, Children's Wisconsin and the Medical College of Wisconsin, Milwaukee, WI 53226, USA. [4]Department of Physiology, Medical College of Wisconsin, Milwaukee, WI 53226, USA. [5]Department of Medicine; Cardiovascular Medicine, University of Wisconsin, Madison, WI 53792, USA. ✉email: rpmccarthy@mcw.edu

Blood rheology models used in cardiovascular CFD simulations are generally classified as Newtonian or non-Newtonian, which can influence the calculation of WSS (i.e., the product of viscosity and near-wall velocity gradients). Viscosity is constant for Newtonian fluids, where the viscous stresses are linearly related to local shear rate. In contrast, viscosity is a function of shear rate for non-Newtonian fluids[7]. Blood is inherently a non-Newtonian, shear thinning fluid with high viscosity at low shear rates and decreasing viscosity as shear rate increases until approximately 200 s^{-1}. The viscosity of blood >200 s^{-1} is generally constant and depends on the hemocrit[7]. Though non-Newtonian viscosity is physiologically more accurate, Newtonian viscosity is easier to implement into CFD simulations. This was explored by Mejia et al. who performed Newtonian and non-Newtonian viscosity simulations in a stented coronary artery to assess the effect on WSS, concluding that the Newtonian approach underestimates WSS within the stented region when compared to the non-Newtonian model[8]. Nevertheless, differences in WSS indices as a result of the viscous model implemented are relatively sparse for patient-specific coronary artery simulations that include branches, physiological boundary conditions, and local stent struts where differences would be expected to be most pronounced.

Inlet boundary conditions for CFD simulations are commonly assumed to be either parabolic or Womersley. Parabolic profiles are characteristic of cylindrical flow where the velocity profile is zero at the wall and increases to a maximum near the centerline. A Womersley profile, however, develops as a result of cyclical (i.e., pulsatile) flow and is characterized by the Womersley number. The Womersley number (α) reflects the ratio of transient inertial forces and viscous forces, and is a function of radius, angular frequency of pulsatile flow, density, and dynamic viscosity. With increased Womersley number, the velocity develops a blunter profile near the center axis. Because of the no-slip condition at the wall, this can in turn influence near-wall velocity gradients and calculation of WSS indices. Myers et al. studied the effect of inlet flow profile within an unbranched unstented right coronary artery (RCA) subjected to steady flow and observed that two diameter distances from the inlet was sufficient for the flow to become statistically identical as observed in local velocity profiles[9].

Additional assumptions applied when conducting stented coronary artery CFD simulations involve the boundary conditions applied at model outlets. This is particularly important for the coronary arteries, where flow and pressure are out-of-phase due to ventricular contraction[10]. Two approaches have been used with this knowledge of physiology in mind, each involving generation of pressure from a network of resistors and capacitors. The 3-element Windkessel lumped parameter network (LPN) has been applied at model outlets for coronary artery simulations with some success[11–13] by realizing that linearity and time invariance can be assumed if the magnitude and duration of an impulse are sufficiently small relative to the duration of the cardiac cycle[14]. Benefits to this approach include simplicity in the determination of Windkessel parameters, each with straightforward physiologic meaning[14]. This was implemented by Gundert et al. in studying differences in WSS resulting from stented patient-specific coronary geometries while demonstrating the applicability of their virtual stenting approach[15]. Ellwein et al. employed a similar approach in modeling outlet boundary conditions but, like Gundert et al., highlight that the model simplifies the contribution of ventricular contraction by scaling the ratio of mean blood pressure and mean flow by 65%, noting that the parameters of the Windkessel model amount to a value ~35% less than the total resistance value in prior work[13,16]. In contrast, a 5-element LPN, which is able to capture the out-of-phase behavior of coronary artery flow and pressure by including elements that account for ventricular contraction[17,18], involves use of less established parameters recently extended to congenital and acquired heart disease[19–21]. Work by Kim et al. provides an overview of the five elements in the model with additional discussion on the derivation of the intramyocardial pressure to capture out-of-phase behavior[17], while Sankaran et al. provide typical values for distributing the coronary resistance[18]. Coogan et al. provide additional details on calculating the values of the resistance parameters from ratios derived from van Huis et al[16,22].

Though some previous studies have modeled outlet boundary conditions using the LPNs mentioned above, to the authors' knowledge, no study to date has directly compared differences in WSS indices between these two coronary artery boundary conditions, or relative to the influence of non-Newtonian flow, for patient-specific stented CFD simulations. Therefore, the object of this investigation was to assess differences in common WSS indices as a result of assumptions often applied with CFD models of stented coronary arteries, focusing on inlet velocity profile, outlet boundary conditions, and the viscosity model.

Methods

Model creation and computation mesh

All protocols were conducted with IRB approval through the Medical College of Wisconsin and in accordance with relevant guidelines and regulations. Informed consent was obtained. Following IRB approval, computed tomography angiography (CTA) and intravascular ultrasound (IVUS) imaging patient data were acquired after stenting of a RCA and used to create a patient-specific reconstruction (Figure 1). The workflow described by Ellwein et al.[13] for use with optical coherence tomography data was applied to the IVUS data obtained in the current case. Briefly, IVUS images were processed to isolate lumen versus stent contours (i.e. segments) by thresholding in MATLAB (Natick, MA). The IVUS imaging wire pullback pathway was then determined by minimizing total bending energy within the CTA volume. Lumen segments were then registered longitudinally on the wire pathway using landmarks and according to the intravascular image spacing. All lumen segments were then oriented orthogonal to the wire pathway and rotated so their centroids were aligned with the vessel centerline. Aligned and oriented segments were then loaded into SimVascular (July 10, 2007 version) for lofting and blending. The stent used clinically (3.0 x 24.0 mm Synergy, Boston Scientific) was recreated in SolidWorks (2024) and then virtually implanted using a series of Boolean operations as previously described by Aleiou[23] and Chiastra[24]. Strut thickness was 79 microns, which was approximately equal to the narrowest strut width.

A boundary layer mesh composed of 16.8 million elements was created with MeshSim^{TM} (www.simmetrix.com) by employing boundary layer meshing to resolve complex flow features around stent struts. This mesh size represented the limit of our computing capabilities both in mesh size (number of elements) and boundary
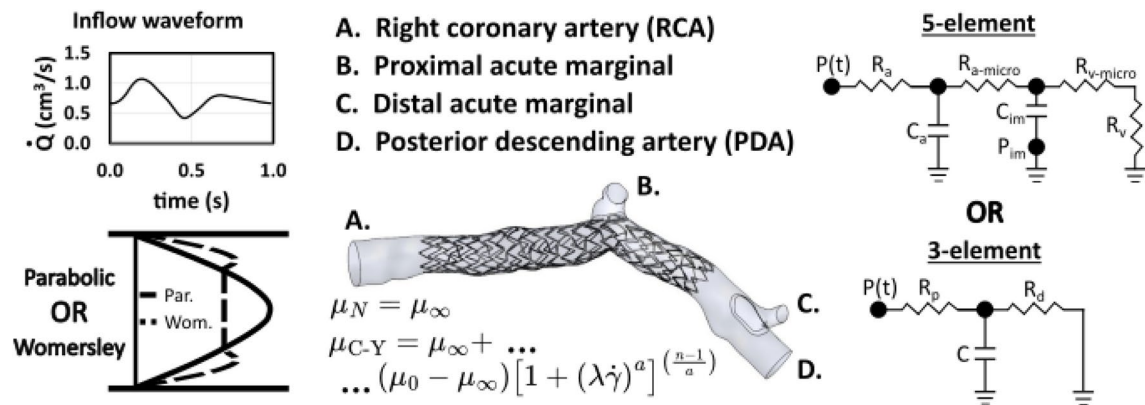
Fig. 1. Overview of the patient-specific stented RCA model and assumptions studied. The RCA model was reconstructed from IVUS and computed tomography. Multiple versions of this model were then subjected to simulations applying assumptions focusing on inlet velocity profile (parabolic or Womersley), outlet boundary conditions (3-element or 5 element), and viscosity model (Newtonian or non-Newtonian) in order to assess differences in common WSS indices.
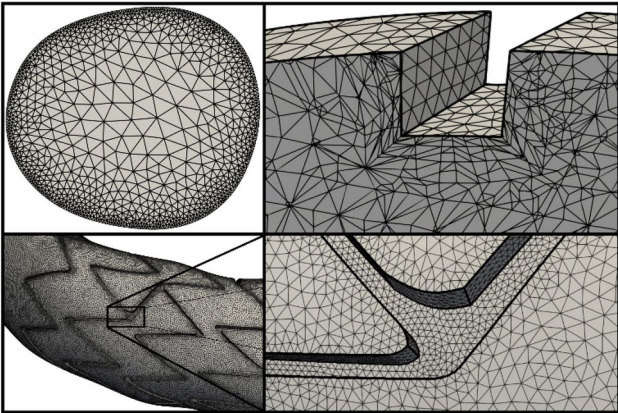
Fig. 2. Boundary layer mesh at inlet (top left), of a cross section containing stent struts (top right), and within representative lumen and stent surfaces (bottom).

Surface	Surface edge length	First layer thickness	Total BL thickness	Number of layers
Lumen	0.045	0.055	0.500	4
Stent	0.020	0.010	0.045	3

Table 1. Boundary layer parameters for the lumen (wall) and stent. Lengths and thicknesses are in *mm*.

layer refinement. Attempts to further refine surface edge length or boundary layer thickness were limited by geometry (stent width and thickness as described below), and computational resources failed to generate a mesh exceeding ~17 million elements. Boundary layer parameters were divided into two categories: stent, and lumen. Stent boundary layer parameters were set to ensure a minimum of four surface elements per strut width, a first boundary layer thickness equal to 1/8 the strut width, and a total boundary layer thickness that was approximately half the strut width and three layers deep. The number of surface elements per strut width was adopted from Kwon et al.[25], who use 2 to 4 elements. For the lumen boundary layer parameters, a surface edge size equal to the total thickness of the stent boundary layer was found to yield the most consistent cell gradient along stent struts where the stent and lumen meet. Four layers was adopted based on the work of Granada[26] and Razavi[27]. Figure 2 shows representations of the mesh at different locations. Detailed mesh parameters are shown in Table 1. The same computational mesh was used for the combination of inlet and outlet boundary conditions studies shown in Figure 1, as described in more detail below.

CFD simulations of stented vasculature can benefit from boundary layer meshing to resolve complex flow features near stent struts. As discussed, this was achieved with MeshSim, which succeeded in meshing stented regions of the geometry where other meshing software failed. MeshSim was compatible with Parasolid ([http

s://plm.sw.siemens.com), but was only able to apply boundary layer mesh parameters for a Parasolid model with named faces. This is relevant as the stent faces created following the Boolean operation to implant the stent were unnamed and therefore needed to first be named in order to be meshed. This was achieved using a custom-built Tool Command Language (TCL) script to identify, name, and number all unnamed faces (e.g. stent_0001, stent_0002, etc.). The newly modified Parasolid model (version 30.0.x) was then opened and resaved with SolidWorks to convert the model to a version and format compatible with MeshSim. Doing so allowed face names and their corresponding surfaces to be recognized. MeshSim was then able to assign boundary layer mesh parameters to all stent and wall-type surfaces (Table 1).

Inflow boundary condition

The inlet velocity flow profile was modeled as parabolic or Womersley ($\alpha = 2.5$) as shown in Figure 1. A calculated cardiac output of 5.56 L/min was determined based on patient height and weight using the body-surface area equation of Mosteller[28] and assumed cardiac index of 2.5 L/min/m². Assuming total coronary artery flow represents 4% of the coronary output[20], an inflow waveform and flow distribution were adopted from healthy RCA flow at rest as reported in Ghorbannia et al.[19]. The waveform was then scaled in time based on patient heart rate (Figure 1).

Outlet boundary conditions

LPNs were applied at model outlets using electrical circuit analogs[17,29]. All outlets for a given simulation used a 3-element Windkessel model that has been applied for simplicity by ignoring the impact of ventricular contraction[24], or an open loop 5-element coronary artery model[20]. The measured systolic (SBP) and diastolic pressures (DBP) were 139 and 63 mmHg, respectively, and were applied as indicated below.

3-Element Windkessel

The 3-element Windkessel electrical circuit analog consists of two resistors and one capacitor. The resistors include a proximal resistance, R_p (sometimes denoted as R_c for characteristic impedance), and a distal resistance, R_d. In the absence of ventricular contraction, the impulse response method of van Huis et al.[16] allows for a 3-element Windkessel approach to be used to conduct coronary artery CFD simulations. In their work, R_p and R_d represent the zero hertz impedance, Z_0, and were ~35% less than the total arterial resistance. This assumed scaling was extended to the current work for its simplicity in implementing 3-element Windkessel LPN boundary conditions for each outlet, knowing that it will yield associated reductions in pressure within simulation results. R_p represents the average impedance of frequencies greater than 7 Hz and was calculated as $R_p = c_{ph}*\rho/(\pi*r^2)$ where c_{ph} is the wave speed, ρ is the blood density, and r is the vessel radius[16]. The wave speed adopted for this study was from canine measurements of Harbaoui et al. and taken as 10.0 m/s[30]. R_d was then calculated as the difference between Z_0 and R_p. Initial arterial compliance for the simulation was estimated from the above calculated resistances and flow rate using a 0D in-house solver to yield pressures that closely match the aimed values. This arterial compliance was then distributed to each branch based on outlet cross-sectional area. The resistance and compliance parameters were then tuned to first achieve aimed outlet flows and then aimed (i.e. scaled) SBP and DBP through an iterative process.

5-Element coronary

The 5-element coronary artery outlet boundary conditions were adapted from the work of Kim et al.[17] and Mantero et al.[29] The model employs three resistors and two capacitors including a coronary arterial resistance (R_a), a coronary arterial microcirculation resistance ($R_{a-micro}$), a coronary venous microcirculation resistance ($R_{v-micro}$), and a coronary venous resistance (R_v), where $R_{v-micro}$ and R_v are in series and therefore summed and collectively denoted as R_v. The resistances sum to equal the total resistance at a given i^{th} outlet ($R_{a,i} + R_{a-micro,i} + R_{v,i} = R_{cor,i}$). Venous resistance was calculated from outlet-specific mean flow and venous pressure, taken as 10 mmHg from Opie[31]. The $R_a:R_{a-micro}$ ratio for each outlet was adopted from the work of van Huis et al.[16] and Burattini et al.[32], where the characteristic impedance and impedance at zero Hertz were used to calculate $R_a/(R_a + R_{a-micro}) = 0.38$ and $R_{a-micro}/(R_a + R_{a-micro}) = 0.62$. The values of R_a and $R_{a-micro}$ were calculated according to the above ratios and from $R_{cor,i} = R_a + R_{a-micro} + R_v$. This approach was likewise employed by Coogan et al.[22].

The protocol used to calculate initial total coronary resistance was adopted from Kim et al.[17], Sankaran et al.[18], and Razavi et al.[21,27]. The total vascular resistance, R_{tot}, was calculated as the quotient of the mean blood pressure (MBP) and aimed coronary artery flow using clinical values of SBP and DBP where MBP = 0.44SBP + 0.56DBP. Murray's law[33], which can be used to relate the resistance of an outlet to its cross-sectional area, was then applied. The outlet cross-sectional areas are shown in Table 2. Given total coronary resistance and outlet cross-sectional areas, resistance at a given (i^{th}) coronary artery outlet is calculated as the total coronary resistance times the sum of the areas of all coronary outlets to the power of 1.3 divided by the area of the given outlet to the power of 1.3: $R_{cor,i} = R_{cor,tot}(\sum_j^n A_j^{1.3})/(A_i^{1.3})$. $R_{cor,i}$ is then distributed into R_a, $R_{a-micro}$, and R_v according to the approach presented by Kim et al.[17] and Sankaran et al.[18], using the ratios shown in Table 3. Resistances were then tuned to first achieve aimed outlet flows and then aimed SBP and DBP in conjunction with adjusting compliance parameters as discussed below.

For the compliance parameters, C_a represents the arterial compliance while C_{im} represents the intramyocardial compliance. The total coronary compliance is adopted from Spaan[34] and scaled to the patient-specific left ventricle mass according to Mizukoshi et al.[35] using the body surface area calculations of Mosteller[28]. The total coronary compliance was then distributed to each outlet based on outlet cross-sectional area. The compliance at each outlet was then divided into the arterial compliance $C_{a,i}$ and intramyocardial compliance $C_{im,i}$ first according to initial ratios provided by Kim et al.[17] and Sankaran et al.[18] before being tuned to the ratios of 0.09

4

		Aout	3-element parameters			5-element parameters				
			R_p	C	R_d	R_a	Ra-micro	R_v	C_a	Cim
Outlet	Proximal acute marginal	0.022	95.75	0.015	757.97	486.35	793.52	89.47	0.041	0.410
	Distal acute marginal	0.015	140.31	0.010	1370.83	873.22	1424.72	131.10	0.028	0.280
	Posterior descending artery	0.072	29.07	0.050	113.32	76.74	125.21	27.17	0.133	1.349

Table 2. Resistance and compliance values for the outlet LPNs. Areas: cm^2; resistances: $10^3 dyn/cm^5$; capacitances: $10^{-6} cm^5/dyn$.

		Ra,i/Rcor,i	Ra-micro,i/Rcor,i	Rv,i/Rcor,i
		---	---	---
Outlet	Proximal acute marginal	0.35	0.58	0.07
	Distal acute marginal	0.36	0.59	0.05
	Posterior descending artery	0.33	0.55	0.12

Table 3. Resistance ratios used in the current study. $R_{cor,i}$ is the total resistance of a given outlet while $R_{a,i}$, $R_{a-micro,i}$, and $R_{v,i}$ are the corresponding arterial, arterial microcirculation, and venous resistances, respectively.

and 0.91, respectively, to achieve aimed pulse pressure and therefore physiologically realistic waveforms. The final tuned values used for each LPN are also summarized in Table 2.

Intramyocardial pressure
The intramyocardial pressure was adapted from available left ventricular pressure (LVP) data in literature[36] and scaled to the patient's SBP assuming an end diastolic pressure of 6 mmHg[19,21]. The intramyocardial pressure waveform P_{im} for the right coronary was then calculated as $P_{im,right}= 0.5LVP$ according to Ghorbannia[19]. The RCA inlet flow and intramyocardial pressure waveforms are aligned according to Barash[37] and Ghorbannia such that RCA flow occurs during both systole and early diastole in the form of two peaks with a local minimum coinciding during early diastole.

## Simulations and results quantification
Simulations were conducted using SimVascular (simvascular.github.io). Blood was assumed to have a density of 1.06 g/cm^3 and viscosity of 0.004 Pa-s (4 cP). Mesh element size required a timestep of 1E-4 s to satisfy the Courant–Friedrichs–Lewy condition. A backflow stabilization coefficient of 0.1 was also applied at model outlets to mitigate divergence of the numerical scheme due to flow reversal. Rigid walls were assumed due to the rigid nature of balloon expandable coronary artery stents and patient diagnosis of coronary artery disease. A no-slip condition was applied to the collective stent and wall surfaces. Preliminary simulations of the coronary artery before virtual stent implantation were run for three cycles for each combination of inlet and outlet boundary condition to tune outlet boundary condition parameters and provide initial conditions for the stented simulations. Residuals were set to 10^{-4} as a convergence criterion. Stented simulations achieved periodicity within two cycles.

There is evidence indicating that spatial and temporal WSS alterations may serve as stimuli for neointimal hyperplasia. Many CFD studies report the oscillatory shear index (OSI), which is a measure of WSS directionality. Lower OSI values indicate that WSS is predominantly oriented in the primary direction of blood flow, whereas a value of 0.5 indicates bi-directional WSS with a time-averaged value of zero. Sites of the vasculature exposed to low WSS magnitude and high OSI are theoretically less likely to experience fluid forces that allow for the washout of noxious and potentially atherogenic materials in contact with the arterial surface (e.g., LDL). Common WSS indices of time-averaged WSS (TAWSS) and OSI were therefore evaluated for the combination of inlet and outlet boundary conditions as shown in Figure 1. Results from the 5-element, Womersley simulation were processed to compare TAWSS from simulations conducted under a Newtonian fluid assumption to those calculated using non-Newtonian viscosity based on the Carreau-Yasuda model[7,38]. This was achieved during post-processing where the shear rate was obtained by dividing TAWSS by dynamic viscosity and substituting the Carreau-Yasuda equation to calculate the corresponding non-Newtonian viscosity and associated TAWSS. The parameters used in the calculation were λ = 1.902 s, n = 0.22, a = 1.25, μ_0 = 0.056 Pa-s, and μ_∞ = 0.004 Pa-s.

Results
Local stent-induced flow patterns
The ring-and-link design of the Synergy stent affects the flow patterns within the intrastrut and near-strut regions. More specifically, the local orientation of the Synergy stent struts relative to the primary flow direction directs blood near struts to develop unique flow patterns depending on whether local velocity vectors are within peak or valley portions of circumferentially repeating rings and their connector link elements. Blood flow velocity vectors near the wall are directed together (i.e. converge) as they enter a valley between stent struts and spread out (i.e. diverge) upon passing over the strut and into an intrastrut region with increasing area (Figure
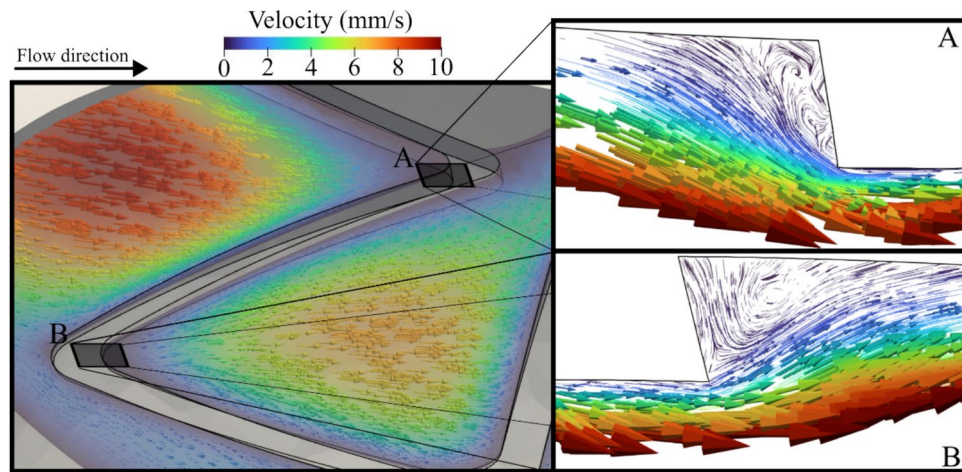
Fig. 3. Velocity vectors as flowing blood approaches valley (A, top right) and peak (B, bottom) stent regions. Forward-facing step geometry and associated streamlines are generally experienced at a stent valley (**A**) while backward-facing step geometry and streamlines are generally experienced at a stent peak (**B**).
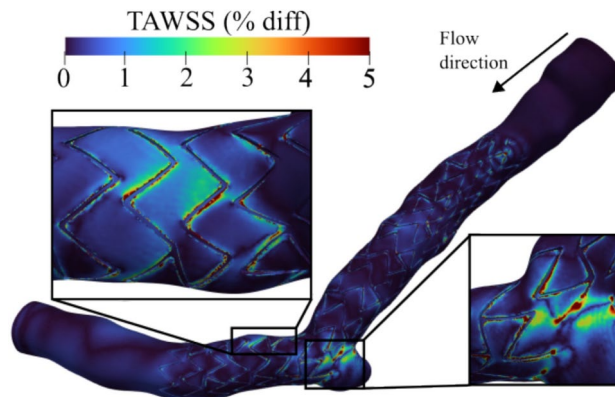
Fig. 4. Difference in time-averaged wall shear stress (TAWSS) between simulations with different outlet boundary conditions. Greatest differences are seen along the inner curvature of the right coronary artery (left) and along stent struts where the stent meets the proximal acute marginal (right).

3). This behavior near struts can be likened to that of forward- and backward-facing step behavior characterized by regions of recirculation and stagnation. Using this analogy, Figure 3A (top) shows a forward-facing step with characteristic flow behavior at the stent valley visualized by streamlines and velocity vectors while Figure 3B (bottom) shows a backward-facing step with similar visualization at the stent peak. Pressure differences due to the imposed outlet boundary condition approaches manifest themselves in the behavior of velocity vectors consistent with this understanding.

Outlet boundary conditions

Percent difference in TAWSS between the 3-element and 5-element outlet boundary conditions for a Womersley inlet profile revealed elevated values adjacent to stent struts, often exceeding 5% when coupled with perturbations induced from the local RCA geometry. This was particularly true in two locations: the first along the angled inner portion of the main curve over the length of three stent rings (Figure 4, left), and the second where the stent intersects with the proximal acute marginal (Figure 4, right).

Percent difference in OSI was elevated throughout the stented region with values exceeding 100% on approximately 50% of the lumen surface (Figure 5). There were also increased values in the intrastrut regions at two main locations: one upstream of the proximal acute marginal, and another along the second ring of the stent. The region upstream of the proximal acute marginal encompassed an area approximately six stent rings longitudinally by four peaks circumferentially, ending once the stent becomes malapposed by the proximal acute marginal. Meanwhile, elevated OSI values along the ring (Figure 5) extend across four of the eight circumferential peaks and show differences of ~200% adjacent to struts and ~100% between struts.

These results were further analyzed by studying instantaneous changes in pressure driving local velocity in regions of stent struts. Instantaneous WSS results that ultimately factored into the TAWSS and OSI results above
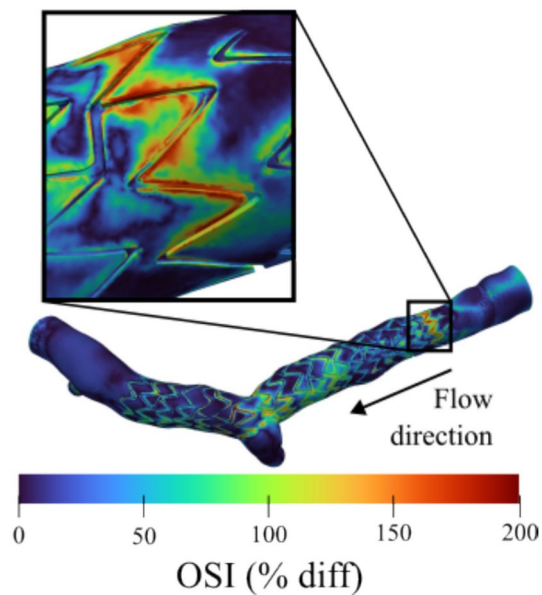
Fig. 5. Oscillatory shear index (OSI) percent difference between 3-element and 5-element outlet LPNs for a Womersley inlet flow profile.

indicated these changes are due to 3-element versus 5-element LPN outlet boundary conditions and their impact on overall pressures during the last cardiac cycle for each case. For example, results from simulations using the Newtonian 3-element versus 5-element LPN outlet boundary conditions (for a Womersley inlet flow profile) show a large decrease in instantaneous pressure near the start of isovolumic relaxation (flow deceleration) which resulted in greater intrastrut velocity differences for the 3-element versus 5-element simulations (Figure 6, A). Similarly, large intrastrut velocity differences between simulations using 3-element versus 5-element LPN outlet boundary conditions can also be seen at a timestep coinciding with flow acceleration (Figure 6, B).

Inlet flow profile
The percent difference in velocity magnitude between parabolic and Womersley inlet profiles at end systole is shown in Figure 7. Slices within a distance equal to twice the inlet diameter are indicated at the bottom of the figure. Velocities between the two inflow profiles becomes negligible by the final slice. For completeness, the same comparison was conducted for the 3-element LPN to consider the effect of the outlet boundary condition on this region. Similar findings were observed, with slices within two diameter distances from the inlet displaying negligible differences in velocity for temporally equivalent regions throughout the cardiac cycle.

Viscosity model
TAWSS calculated using non-Newtonian versus Newtonian viscosities revealed the greatest percent difference (often exceeding 100%) adjacent to stents struts. Representative results are shown for the 5-element LPN and Womersley inlet flow profile in Figure 8 (left) alongside a plot of the non-Newtonian and Newtonian viscosity as a function of shear rate (Figure 8; right). Differences at locations greater than one strut width away from the stent rarely exceeded 10%. In considering that the non-Newtonian viscosity model employed in this analysis has the greatest effect for shear rates $< 100 \text{ s}^{-1}$, analysis of the shear rate for a threshold range of 0 to 100 s^{-1} from simulations using 3-element and 5-element LPN outlet boundary conditions with Womersley inlet profile shows regions of instantaneous low shear rate ($< 100 \text{ s}^{-1}$) differ slightly for the 3-element and 5-element simulations, and there is a strong overlap between these regions and regions of increased TAWSS percent difference. Importantly, these regions of low shear rate differences coincide with the near-strut regions and bifurcations most susceptible to differences in instantaneous pressure gradients, and therefore velocity differences and WSS indices, between results stemming from differing outlet boundary conditions illustrated in Figure 6. These differences in shear rate for the 3-element and 5-element LPN outlet boundary condition simulations are masked in the cycle-averaged quantity of TAWSS.

Discussion
Coronary artery CFD simulations are subject to assumptions implemented in the process and inherent tradeoffs are adopted by personnel conducting the simulations. These assumptions can impact results and influence conclusions drawn about the indices of interest. For example, WSS indices commonly used in assessing likelihood of restenosis or late stent thrombosis are particularly susceptible to the assumptions employed. In order to assess the influence of several common assumptions, distinct sets of simulations were performed to compare results from assumptions involved in modeling the inlet velocity profile, the LPN used to model outlet boundary conditions, and the blood rheology model. There are four main findings from this study. First, differences in
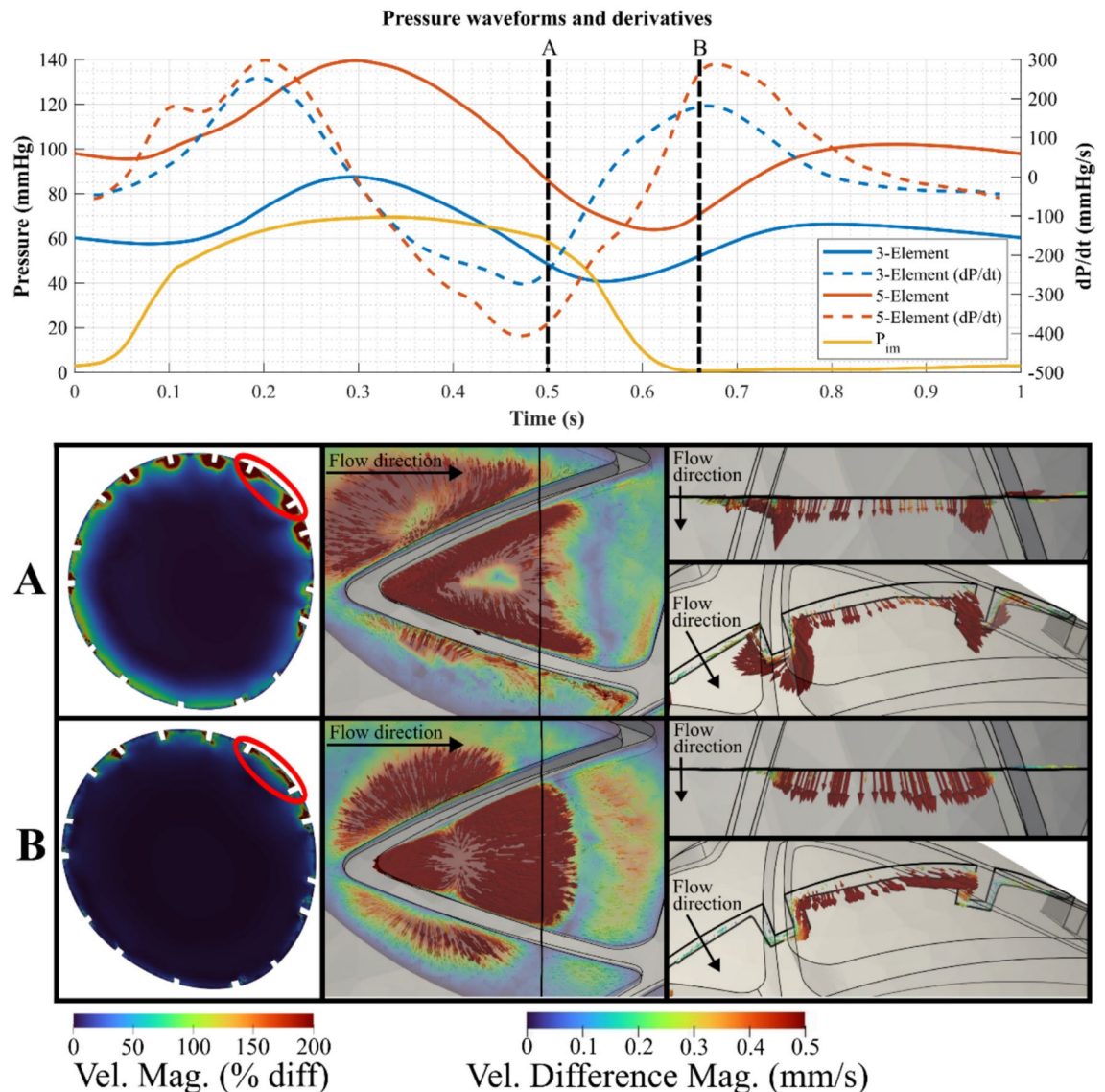
Fig. 6. Top: Pressure waveform results from simulations using 3-element and 5-element LPN outlet boundary conditions (blue and orange solid lines, respectively) with Womersley inlet flow profile, pressure gradient of the 3-element and 5-element pressure waveforms (blue and orange dashed lines, respectively), and intramyocardial pressure from the 5-element LPN (yellow line). The location shown corresponds to the region of elevated OSI in Fig. 5, which is two diameter distances from the inlet. Bottom: Enhanced cross-sectional view showing velocity magnitude percent difference at timepoints A and B (left). Differences in velocity magnitude were calculated by subtracting velocities of the 3-element LPN outlet boundary condition simulation from those of the 5-element LPN outlet boundary condition generally within the red ellipse. Velocity differences between the 5-element and 3-element LPN outlet boundary condition simulations are shown for vectors and contours located at a depth of approximately half the strut thickness below the lumen surface (middle) and in cross-section (right).

velocity between parabolic and Womersley ($\alpha = 2.5$) inlet flow profiles beyond a distance of two diameters from the inlet were negligible. Second, the percent difference between 3-element Womersley and 5-element coronary artery outlet boundary condition LPNs for TAWSS and OSI were up to 5 and 200%, respectively. Greatest differences occurred near stent struts, but some intrastrut regions also showed OSI percent difference of 100%. Overall, OSI calculations were more sensitive to changes in outlet LPN model. Third, changes in instantaneous pressure and their associated local velocity and WSS indices were a result of the employed outlet boundary conditions and their impact during the cardiac cycle. Fourth, Newtonian vs. non-Newtonian calculations confirmed that the greatest TAWSS percent difference between the two viscosity models occurs adjacent to stent struts, where percent difference often exceeded 100%. Each of these is discussed in more detail below.

In this work we compared the influence of parabolic and Womersley inflow profiles to illustrate the difference in near-wall velocity gradients and the distance required before differences become negligible. We conducted
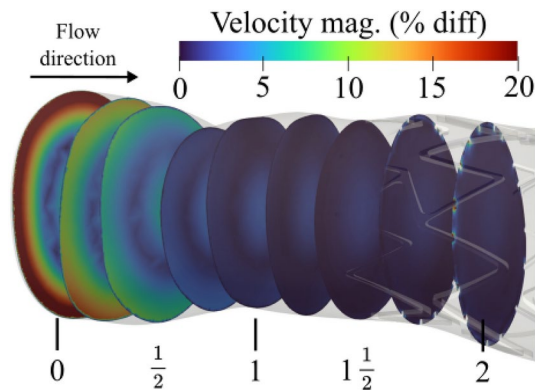
Fig. 7. Velocity magnitude percent difference due to parabolic and Womersley ($\alpha = 2.5$) inlet flow profiles during late systole. Cross-sections two full inlet diameter distances from the inlet at quarter slice increments are shown. The inlet is located at cross-Sect. 0.
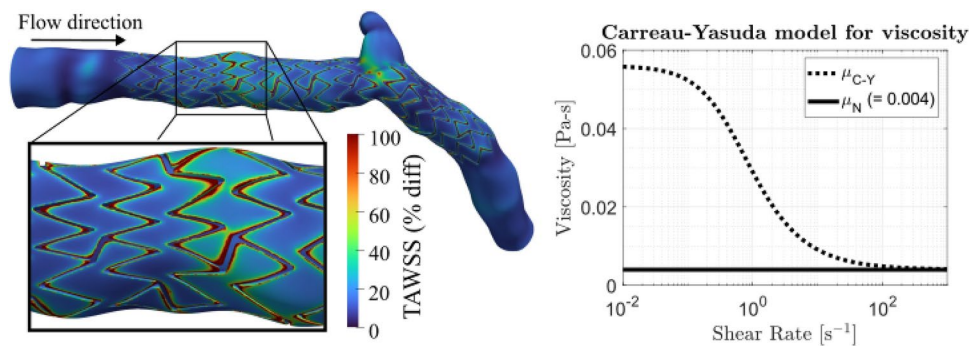
Fig. 8. Left: Time-averaged wall shear stress (TAWSS) percent difference between the two viscosity models for a 5-element LPN and Womersley inlet flow profile. Right: Comparison of the Newtonian and non-Newtonian (Carreau-Yasuda) viscosity models implemented. Parameters used for the calculation are given in Sect. "Simulation and Results Quantification".

simulations that differ only in inlet velocity profile to illustrate these differences. We showed that the choice of inlet velocity profile affects the velocity profiles within two diameter distances distal to the inlet, and that beyond this distance the differences become negligible. This agrees with the work by Myers et al.[9] who explored the influence and development of parabolic, Womersley, blunt, and skewed inlet velocity profiles to find that WSS differences beyond a distance of two diameters from the inlet were negligible. Despite a difference in Womersley number (current: $\alpha = 2.5$; Myers et al. $\alpha = 1.82$), the current study extends the findings of the prior work by considering a stented artery and inclusion of associated branches. Given the influence of the velocity gradient in calculating WSS indices and the distance required before differences become negligible, conclusions regarding WSS indices are less impacted by inflow assumptions if made beyond 2 diameters downstream of the inlet.

We conducted simulations using 3-element Windkessel and 5-element coronary LPN outlet boundary conditions to compare the effect of ignoring ventricular contraction in stented coronary artery simulations. The 3-element LPN outlet boundary conditions stimulations simply ignore the contribution of ventricular contraction and are therefore unable to model the out-of-phase behavior of pressure and flow. Conversely, this contribution is built into the 5-element model, which incorporates the influence of intramyocardial pressure. Contours of percent difference in velocity at the location of greatest OSI difference show elevated values at timepoints of large increase or decrease in instantaneous pressure. The regions of high OSI percent differences correlate with the severity of velocity differences.

The flow patterns within the intrastrut and near-strut regions are consistent with prior descriptions from other stent geometries[39–41]. Forward- and backward-facing steps in blood flow promote procoagulant conditions due to the nature of the convective acceleration-deceleration and recirculation regions[39]. Namely, accelerated flow at the exposed stent corners may result in elevated shear stress, which can lead to platelet activation. This can result in the activated platelets washing downstream into the separation zone where they can reach critical concentrations for the coagulation cascade. This is exacerbated by the removal of endothelium during stenting, which can expose the highly thrombogenic extracellular matrix surface and eliminate associated anticoagulant mechanisms.

As motivated in the methods section, adopting the impulse-response method of van Huis et al.[16] when applying 3-element Windkessel LPN outlet boundary conditions for coronary artery CFD simulations entails

scaling the impedance by ~35%. A consequence of doing so is a decreased pressure range relative to simulation results using the 5-element LPN outlet boundary condition approach. For example, at timepoint A of Figure 6, differences in instantaneous pressure between 3-element and 5-element LPN outlet boundary conditions at the start of isovolumic relaxation (flow deceleration) resulted in greater intrastrut velocity differences. Similarly, timepoint B shows a large increase in instantaneous pressure between the two outflow boundary conditions, which corresponds to associated velocity differences. This illustrates the influence of the intramyocardial pressure and corresponding out-of-phase behavior of the pressure and flow waveforms between simulations differing only in outlet boundary condition type. When coupling these WSS results with the importance of capturing out-of-phase behavior of coronary flow and the inability of the 3-element approach to do so, it stands to reason that 5-element LNP outlet boundary conditions are preferred between the two. It is also worth noting that the current simulations were conducted using data from a stented RCA, where the out-of-phase nature of coronary artery blood flow and pressure have been shown to be less pronounced relative to findings in the left anterior descending and circumflex coronary arteries[19]. Hence, the differences presented here are likely to be more pronounced if comparing results of 3-element versus 5-element LPN outlet boundary conditions from stented CFD simulations in these arteries, although this hypothesis remains to be tested.

Newtonian versus non-Newtonian TAWSS results demonstrate greatest TAWSS percent differences occur adjacent to stent struts. This finding agrees with the work of Mejia et al.[8], who perform comparison studies between Newtonian and non-Newtonian viscosity models of an idealized stented coronary geometry. Two Newtonian models are used in their study, one using 3.5 cP viscosity and the other using 4.7 cP calculated using the Carreau-Yasuda model, but assuming an average strain rate in a coronary artery. They noted that the 4.7 cP value resulted in higher WSS but still underestimated the value in near-stent regions when compared to the non-Newtonian model. They concluded that it is more appropriate to use non-Newtonian models to predict WSS indices within stented arterial segments. Similar work is performed by Karanasiou et al.[42] in which Newtonian and non-Newtonian simulations were conducted from a stented (Synergy) patient-specific model of the left anterior descending artery constructed with optical coherence tomography and angiography data. Comparison of WSS along the longitudinal direction of each model shows similar WSS patterns in that, for each case, the non-Newtonian model produced higher WSS values than the Newtonian model, and that elevated values occurred adjacent to stent struts. WSS values between these studies and the current work differ, but the use of steady state versus transient inlet conditions may account for this difference. Collectively, the current and prior studies show Newtonian viscosity models underestimate WSS and should be avoided in favor of non-Newtonian models when possible.

The current results should be interpreted relative to several potential limitations. First, the current study only considered data from one patient. Comparison studies involving multiple patients may provide additional guidance regarding the assumptions evaluated and their influence on WSS indices. Second, our study was limited to the analysis of a single stent within the RCA, which experiences different intramyocardial pressure than the left coronary artery bed as mentioned above. Third, the current study assumes a rigid stent and artery wall. While the data used was from a patient who had coronary artery disease known to cause arterial stiffening and the stent is also likely rigid[43], considering proximal, distal and intrastrut deformation of the RCA during the cardiac cycle via fluid-structure interaction simulations could result in slightly lower WSS values due to artery deformation, although at the expense of computationally time. Fourth, the current study did not involve structural finite element analysis to perform stent implantation, which could be more accurate if precise material properties of the stenosed coronary artery were known according to recent methods[44]. Unfortunately, such material property data were not available for the current patient and a fluid-structure interaction simulation would be computationally expensive. A compromise between rigid wall simulations and stent deformation was therefore applied here based on a patient specific method originally applied by Gundert et al.[15]. This method has since been applied for patient-specific models and from idealized and patient-specific intravascular imaging of coronary arteries post-stenting[11,13,25]. Fifth, though the current work extended the stented coronary artery reconstruction methods from Ellwein et al.[13] to IVUS, geometry has a large impact on WSS distributions, and user variability in this process should ultimately be assessed relative to the assumptions studied moving forward. Sixth, the current work did not model non-Newtonian flow during the simulation. Thus, the cumulative effects of a different viscosity model during the cardiac cycle were not captured. Finally, the simulations presented in this study were not directly validated *in vitro* or *in vivo*. Validation of patient-specific CFD simulation results is inherently difficult since the vasculature of interest cannot be removed and is exposed to physiologic loading that is difficult to mimic *ex vivo*. Moreover, transducers used to measure blood flow and pressure can also impact such measurements by their presence within or around the flow domain. Hence, simulations in the current proposal were validated to the extent possible by reproducing clinical observations within the error of established clinical tools, minimizing uncertainty in the input data to the extent possible, and being transparent about how assumptions could lead to disparity in the results obtained. Nevertheless, SimVascular has been validated in prior studies, notably in an *in vitro* study of patient-specific coronary aneurysm anatomy of Kawasaki disease derived from phase contrast MRI[45]. The authors compare velocity contours and profiles obtained from CFD to those measured in a physical phantom created from the same MRI data, demonstrating that SimVascular is capable of producing qualitative and quantitative predictions of velocities with excellent agreement when compared to the experimental results. It is also worth noting that, although the goal of the authors was to validate SimVascular in general, the anatomy and flow conditions considered in their work pertain to the coronary arteries, which were also the focus of the present study. Validation of numerical simulation methods to model blood flow with a clinical treatment approach has additionally been done using similar methods[46].

The current IVUS-based patient-specific stented RCA study reveals the importance in choosing appropriate assumptions when conducting CFD simulations of stented coronary arteries. Insight into these assumptions can better inform future patient-specific numerical models of blood flow and may ultimately yield improved patient

outcomes in the clinical setting for approaches that rely on WSS indices. Given the relationship of WSS indices in predicting regions susceptible to restenosis, it is somewhat concerning that model results for TAWSS or OSI can differ by as much as 100–200% from a single assumption. Of note are the differences stemming from the choice of outlet boundary conditions. The 3-element LPN model adapted from literature, although simple to implement, cannot replicate the out-of-phase nature between pressure and flow in the coronary arteries since it ignores intramyocardial pressure. Differences in WSS indices presented in Figures 4 and 5 are due to changes in velocity profiles in the model, and are a manifestation of neglecting ventricular contraction, resulting in different pressure gradients during the cardiac cycle as illustrated in Figure 6. Differences near the inlet due to the prescribed velocity profile were expected and consistent with prior literature[9] since the two types of velocity profiles impose different velocity gradients at the wall thereby resulting in different WSS values. Analysis of differences in velocity between subsequent cycles for a given inlet profile shows that any downstream differences are likely due to turbulent kinetic energy rather than the inlet profile. These can be minimized to some degree with highly resolved meshes and additional cardiac cycles, but are nonetheless an inherent part of the features developing under complex flow conditions. The choice of viscosity model also affects the WSS indices in the stented region, which agrees with the established literature[7,8,42,47]. This highlights a need for flow solvers to include non-Newtonian models, particularly when characterizing stent-induced differences in WSS indices. Collectively, the current results suggest that certain assumptions commonly applied for simulations of stented coronary arteries have a greater impact on TAWSS and OSI than others, with outlet boundary conditions being paramount, followed by viscosity model and inlet velocity profile.

Data availability

Datasets used and/or analyzed during the current study cannot be publicly shared due to privacy restrictions. Requests to access the datasets and/or computational models should be directed to the corresponding author.

References

1. Yeo, K. K. et al. Contemporary clinical characteristics, treatment, and outcomes of angiographically confirmed coronary stent thrombosis: results from a multicenter California registry. *Catheter. Cardiovasc. Interv.* **79**, 550–556 (2012).
2. Bønaa, K. H. et al. Drug-eluting or bare-metal stents for coronary artery disease. *N. Engl. J. Med.* **375**, 1242–1252 (2016).
3. Koskinas, K. C., Chatzizisis, Y. S., Antoniadis, A. P. & Giannoglou, G. D. Role of endothelial shear stress in stent restenosis and thrombosis: pathophysiologic mechanisms and implications for clinical translation. *J. Am. Coll. Cardiol.* **59**, 1337–1349 (2012).
4. Joner, M. et al. Pathology of drug-eluting stents in humans: Delayed healing and late thrombotic risk. *J. Am. Coll. Cardiol.* **48**, 193–202 (2006).
5. Kotani, J. et al. Incomplete neointimal coverage of sirolimus-eluting stents: Angioscopic findings. *J. Am. Coll. Cardiol.* **47**, 2108–2111 (2006).
6. Finn, A. V. et al. Vascular responses to drug eluting stents: importance of delayed healing. *Arterioscler. Thromb. Vasc. Biol.* **27**, 1500–1510 (2007).
7. Cho, Y. I. & Kensey, K. R. Effects of the non-Newtonian viscosity of blood on flows in a diseased arterial vessel. Part 1: Steady flows. *Biorheology* **28**, 241–262 (1991).
8. Mejia, J., Mongrain, R. & Bertrand, O. F. Accurate prediction of wall shear stress in a stented artery: Newtonian versus non-newtonian models. *J. Biomech. Eng.* **133**, 74501 (2011).
9. Myers, J. G., Moore, J. A., Ojha, M., Johnston, K. W. & Ethier, C. R. Factors influencing blood flow patterns in the human right coronary artery. *Ann. Biomed. Eng.* **29**, 109–120 (2001).
10. Bovendeerd, P. H. M., Borsje, P., Arts, T. & van De Vosse, F. N. Dependence of intramyocardial pressure and coronary flow on ventricular loading and contractility: A model study. *Ann. Biomed. Eng.* **34**, 1833–1845 (2006).
11. Gundert, T. J., Dholakia, R. J., McMahon, D. & LaDisa, J. F. Computational fluid dynamics evaluation of equivalency in hemodynamic alterations between driver, integrity, and similar stents implanted into an idealized coronary artery. *J. Med. Device* **7**, 11004 (2013).
12. Williams, A. R., Koo, B.-K., Gundert, T. J., Fitzgerald, P. J. & LaDisa, J. F. Jr. Local hemodynamic changes caused by main branch stent implantation and subsequent virtual side branch balloon angioplasty in a representative coronary bifurcation. *J. Appl. Physiol.* **109**, 532–540 (2010).
13. Ellwein, L. M. et al. Optical coherence tomography for patient-specific 3D artery reconstruction and evaluation of wall shear stress in a left circumflex coronary artery. *Cardiovasc. Eng. Technol.* **2**, 212–227 (2011).
14. LaDisa, J. F. Jr. et al. Computational simulations for aortic coarctation: Representative results from a sampling of patients. *J. Biomech. Eng.* **133**, 91008 (2011).
15. Gundert, T. J. et al. A rapid and computationally inexpensive method to virtually implant current and next-generation stents into subject-specific computational fluid dynamics models. *Ann. Biomed. Eng.* **39**, 1423–1437 (2011).
16. Van Huis, G. A., Sipkema, P. & Westerhof, N. Coronary input impedance during cardiac cycle as determined by impulse response method. *Am. J. Physiology-Heart Circ. Physiol.* **253**, H317–H324 (1987).
17. Kim, H. J. et al. Patient-specific modeling of blood flow and pressure in human coronary arteries. *Ann. Biomed. Eng.* **38**, 3195–3209 (2010).
18. Sankaran, S. et al. Patient-specific multiscale modeling of blood flow for coronary artery bypass graft surgery. *Ann. Biomed. Eng.* **40**, 2228–2242 (2012).
19. Ghorbanniahassankiadeh, A., Marks, D. S. & LaDisa, J. F. Correlation of Computational Instantaneous Wave-Free Ratio With Fractional Flow Reserve for Intermediate Multivessel Coronary Disease. *J. Biomech. Eng.* https://doi.org/10.1115/14049746 (2021).
20. Razavi, A., Sachdeva, S., Frommelt, P. C. & LaDisa, J. F. Jr. Patient-specific numerical analysis of coronary flow in children with intramural anomalous aortic origin of coronary arteries. *Semin. Thorac. Cardiovasc. Surg.* **33**, 155–167 (2021).
21. Razavi, A., Sachdeva, S., Frommelt, P. C. & LaDisa, J. F. Jr. Computational assessment of hemodynamic significance in patients with intramural anomalous aortic origin of the coronary artery using virtually derived fractional flow reserve and downstream microvascular resistance. *J. Biomech. Eng.* **144**, 31005 (2022).
22. Coogan, J. S., Humphrey, J. D. & Figueroa, C. A. Computational simulations of hemodynamic changes within thoracic, coronary, and cerebral arteries following early wall remodeling in response to distal aortic coarctation. *Biomech. Model. Mechanobiol.* **12**, 79–93 (2013).

23. Aleiou, A. A. Evaluating Wall Shear Stress Indices to Uncover Stimuli for Restenosis and Malapposition in Stented Coronary Arteries. (Marquette University, 2017).
24. Chiastra, C. et al. Computational replication of the patient-specific stenting procedure for coronary artery bifurcations: From OCT and CT imaging to structural and hemodynamics analyses. *J. Biomech.* **49**, 2102–2111 (2016).
25. Kwon, S., Feinstein, J. A., Dholakia, R. J. & LaDisa, J. F. Quantification of local hemodynamic alterations caused by virtual implantation of three commercially available stents for the treatment of aortic coarctation. *Pediatr. Cardiol.* **35**, 732–740 (2014).
26. Blanch Granada, A. et al. Hemodynamic evaluation of Norwood aortic arch geometry compared to native arch controls. *J. Biomech. Eng.* **147**, 1–36 (2025).
27. Razavi, A. Patient-Specific Modeling of Altered Coronary Artery Hemodynamics to Predict Morbidity in Patients with Anomalous Origin of a Coronary Artery. (Marquette University, 2020).
28. Mosteller, R. Simplified calculation of body surface area. *N. Engl. J. Med.* **317**, 1098 (1987).
29. Mantero, S., Pietrabissa, R. & Fumero, R. The coronary bed and its role in the cardiovascular system: A review and an introductory single-branch model. *J. Biomed. Eng.* **14**, 109–116 (1992).
30. Harbaoui, B., Courand, P.-Y., Cividjian, A. & Lantelme, P. Development of coronary pulse wave velocity: New pathophysiological insight into coronary artery disease. *J. Am. Heart Assoc.* **6**, e004981 (2017).
31. Opie, L. H. *Heart Physiology: From Cell to Circulation.* (Lippincott Williams & Wilkins, 2004).
32. Burattini, R., Sipkema, P., van Huis, G. A. & Westerhof, N. Identification of canine coronary resistance and intramyocardial compliance on the basis of the waterfall model. *Ann. Biomed. Eng.* **13**, 385–404 (1985).
33. Zamir, M., Sinclair, P. & Wonnacott, T. H. Relation between diameter and flow in major branches of the arch of the aorta. *J. Biomech.* **25**, 1303–1310 (1992).
34. Spaan, J. A. Coronary diastolic pressure-flow relation and zero flow pressure explained on the basis of intramyocardial compliance. *Circ. Res.* **56**, 293–309 (1985).
35. Mizukoshi, K. et al. Normal values of left ventricular mass index assessed by transthoracic three-dimensional echocardiography. *J. Am. Soc. Echocardiogr.* **29**, 51–61 (2016).
36. Hayabuchi, Y., Ono, A., Homma, Y. & Kagami, S. Analysis of right ventricular myocardial stiffness and relaxation components in children and adolescents with pulmonary arterial hypertension. *J. Am. Heart Assoc.* **7**, e008670 (2018).
37. Barash, P. G. *Clinical Anesthesia.* (Lippincott Williams & Wilkins, 2009).
38. Yasuda, Kenji. Investigation of the Analogies Between Viscometric and Linear Viscoelastic Properties of Polystyrene Fluids. (Massachusetts Institute of Technology, 1979).
39. Jiménez, J. M. & Davies, P. F. Hemodynamically driven stent strut design. *Ann. Biomed. Eng.* **37**, 1483–1494 (2009).
40. Prabhu, S. et al. Engineering assessment of the longitudinal compression behaviour of contemporary coronary stents. *EuroIntervention* **8**, 275–281 (2012).
41. LaDisa, J. F. et al. Three-dimensional computational fluid dynamics modeling of alterations in coronary wall shear stress produced by stent implantation. *Ann. Biomed. Eng.* **31**, 972–980 (2003).
42. Karanasiou, G. E. *et al.* A proof-of-concept study for the simulation of blood flow in a post arterial segment for different blood rheology models. in *2022 44th Annual International Conference of the IEEE Engineering in Medicine & Biology Society (EMBC)* 3985–3988 (2022).
43. LaDisa, J. F. Jr. et al. Stent implantation alters coronary artery hemodynamics and wall shear stress during maximal vasodilation. *J. Appl. Physiol.* **93**, 1939–1946 (2002).
44. Ghorbannia, A. & LaDisa, J. F. Jr. Intravascular imaging of angioplasty balloon under-expansion during pre-dilation predicts hyperelastic behavior of coronary artery lesions. *Front. Bioeng. Biotechnol.* **11**, 1192797 (2023).
45. Kung, E., Kahn, A. M., Burns, J. C. & Marsden, A. In vitro validation of patient-specific hemodynamic simulations in coronary aneurysms caused by Kawasaki disease. *Cardiovasc. Eng. Technol.* **5**, 189–201 (2014).
46. Ku, J. P. et al. In vivo validation of numerical prediction of blood flow in arterial bypass grafts. *Ann. Biomed. Eng.* **30**, 743–752 (2002).
47. Benard, N., Perrault, R. & Coisne, D. Computational approach to estimating the effects of blood properties on changes in intra-stent flow. *Ann. Biomed. Eng.* **34**, 1259–1271 (2006).

Acknowledgements

Author contributions

R.P.M. built the computational models, performed simulations, analyzed results, and drafted the manuscript. J.F.L. served as principal investigator and led design and conception of the study. P.J.M. and D.S.M. performed acquisition of clinical data. All authors contributed to interpretation and analysis of results as well as authorship and revision of the manuscript.

Declarations

Competing interests

The authors declare that they have no competing interests.

Additional information

Correspondence and requests for materials should be addressed to R.P.M.

Reprints and permissions information is available at www.nature.com/reprints.

Publisher's note Springer Nature remains neutral with regard to jurisdictional claims in published maps and institutional affiliations.